Title	Reverse water-gas shift reaction over Pt/MoOx/TiO2 : reverse Mars-van Krevelen mechanism via redox of supported MoOx
Author(s)	Mine, Shinya; Yamaguchi, Taichi; Ting, Kah Wei; Maeno, Zen; Siddiki, S. M. A. Hakim; Oshima, Kazumasa; Satokawa, Shigeo; Shimizu, Ken-ichi; Toyao, Takashi
Citation	Catalysis science and technology, 11(12), 4172-4180 https://doi.org/10.1039/d1cy00289a
Issue Date	2021-06-21
Doc URL	http://hdl.handle.net/2115/86024
Type	article (author version)
File Information	Main text_PtMoOxTiO2_RWGS_CST_revised.pdf

Reverse water-gas shift reaction over Pt/MoO$_x$/TiO$_2$:

reverse Mars-van Krevelen mechanism via redox of supported MoO$_x$

Shinya Mine,[a] Taichi Yamaguchi,[a] Kah Wei Ting,[a] Zen Maeno,[a] S. M. A. Hakim Siddiki,[a]

Kazumasa Oshima,[b] Shigeo Satokawa,[b] Ken-ichi Shimizu,*[a,c] Takashi Toyao,*[a,c]

[a] Institute for Catalysis, Hokkaido University, N-21, W-10, Sapporo 001-0021, Japan

[b] Department of Materials and Life Science, Faculty of Science and Technology, Seikei University, Musashino, Tokyo 180-8633, Japan

[c] Elements Strategy Initiative for Catalysts and Batteries, Kyoto University, Katsura, Kyoto 615-8520, Japan

*Corresponding authors

Ken-ichi Shimizu, Takashi Toyao

E-mail: kshimizu@cat.hokudai.ac.jp, toyao@cat.hokudai.ac.jp

Abstract

The reverse water-gas shift (RWGS) reaction is a promising catalytic route for reducing CO_2 emissions because its product, CO, is a key intermediate in various industrialized catalytic processes that produce fuels and chemicals. We describe herein a MoO_x/TiO_2-supported Pt catalyst ($Pt(3)/MoO_x(15)/TiO_2$; Pt loading = 3 wt%, MoO_3 loading = 15 wt%) that promotes the RWGS reaction at low temperature (200-300 ˚C) with high activity and selectivity. The catalytic performance for both CO_2 conversion and selectivity of $Pt(3)/MoO_X(15)/TiO_2$ is better than those of Pt catalysts on other supports and other metal catalysts supported on $MoO_X(15)/TiO_2$, as well as Cu- and Fe-Cr-based industrial catalysts. Moreover, results of *operando* X-ray absorption spectroscopy studies show that the reaction takes place via reverse Mars−van Krevelen mechanism where H_2 acts as a reducing agent to create oxygen vacancies on the supported Mo oxide species that are filled by CO_2 as an oxidizing agent.

Keywords: $Pt/MoO_X/TiO_2$, Reverse-water gas shift (RWGS), *operando* X-ray absorption spectroscopy (XAS), reverse Mars-van Krevelen mechanism, oxygen vacancy

Introduction

Accumulation of a large amount of CO_2 as a greenhouse gas negatively impacts the global environment. Thus, the development of efficient catalytic processes to obtain value-added chemicals from CO_2 as a C1 source is strongly desired to suppress CO_2 emission and decrease the concentration of atmospheric CO_2.[1–6] Among various methods, catalytic hydrogenation using H_2 as a reductant is one of the most extensively studied processes and it could be the key for the vast utilization of CO_2 if a carbon-neutral and economically viable source of H_2 can be developed.[7–11] The catalytic hydrogenation of CO_2 produces several important bulk chemicals including formic acid, methanol, and hydrocarbons.[12,13,22–24,14–21] Although this one-step CO_2 conversion to value-added chemicals is attractive, there is difficulty associated with the fact that CO_2 is kinetically unreactive and thermodynamically stable.[25,26]

The catalytic hydrogenation of CO_2 to CO, also called the reverse water-gas shift (RWGS: $CO_2 + H_2 \rightarrow CO + H_2O$) reaction, serves as a highly flexible strategy for utilization of CO_2 because CO is an important intermediate in various well-established catalytic processes to manufacture value-added chemicals.[27] These processes include alcohol synthesis,[28,29] Fischer-Tropsch (FT) synthesis,[30,31] and other high-value-added product formation reactions.[32] Considerable effort has been devoted to developing efficient heterogeneous RWGS catalysts.[33,34,43,35–42] In particular, many studies have been conducted to develop and improve high-temperature RWGS processes (typically above 300 ˚C).[42] One reason for this is that the RWGS reaction is endothermic, namely,

high-temperature reaction conditions are favored to obtain high one-pass CO yields. However, process operations at high temperatures are not always feasible in real-world applications especially for future chemical plants where on-site/distributed systems are desired, and thus, developments of low-temperature RWGS catalysts are of vital importance. Despite its demands in industry, only limited effort has been devoted to the low-temperature RWGS process, and the CO formation rate and the selectivity toward CO over CH_4 still needs to be improved to meet the criteria for implementation in industry (see **Table S1** in the Supporting Information for reported RWGS performances ($T \leq 250$ °C)). Although other interesting approaches employing photothermal catalysis[44–48] that operate at relatively low temperatures have also been examined in recent years, they require an external light source that hinder industrial scale applications and often still suffer from low activities.[49] Therefore, it is clear that designing and synthesizing more efficient standard thermal catalysts for the RWGS reaction, together with understanding the precise nature of the catalysts are highly important.

In the present study, we used Pt nanoparticles supported on MoO_x/TiO_2 ($Pt(3)/MoO_x(15)/TiO_2$; Pt loading = 3 wt%, MoO_3 loading = 15 wt%) as a catalyst for the RWGS reaction at temperature range of 200-300 ˚C. This $Pt/MoO_x/TiO_2$ type catalysts are known to exhibit high catalytic performance for various hydrogenation reactions including carboxylic acid hydrogenation,[50,51] methylamine synthesis from $CO_2/H_2/NH_3$,[52] and low-temperature methanol production from CO_2/H_2.[53] We found that the $Pt(3)/MoO_x(15)/TiO_2$ catalyst is also effective for CO production. The reaction mechanism was examined with *operando* X-ray absorption spectroscopy (XAS).

Results and discussion

Structural analysis of Pt(3)/MoO$_x$(15)/TiO$_2$

Pt(3)/MoO$_x$(15)/TiO$_2$ was produced through sequential impregnation employing TiO$_2$ (P25, 50 m^2/g), (NH$_4$)$_6$Mo$_7$O$_{24}$·4H$_2$O, and Pt(NH$_3$)$_2$(NO$_3$)$_2$, and subsequent H$_2$ reduction at 300 °C (Please see the electronic supplementary information for detailed preparation condition). The XRD pattern for TiO$_2$ has peaks originating from both rutile and anatase phases (**Figure S1**). The Mo oxide species in MoO$_3$(15)/TiO$_2$ exists as MoO$_3$. Peaks from MoO$_3$ were also observed in the XRD pattern for the unreduced sample (PtO$_2$(3)/MoO$_3$(15)/TiO$_2$), which decreased after the H$_2$ reduction treatment. It is important to note that peaks associated with Pt were not seen in the patterns. The BET specific surface areas (S$_{BET}$) of MoO$_3$(15)/TiO$_2$ and Pt(3)/MoO$_x$(15)/TiO$_2$ were determined by performing N$_2$ adsorption isotherms to be 44 and 43 m^2/g, respectively.

In order to examine the particle sizes and morphologies of the introduced Pt and Mo species, bright-field (BF) and high-angle annular dark-field scanning transmission electron microscopy (HAADF-STEM) observations were made (**Figure 1**). For images of TiO$_2$ and MoO$_3$(15)/TiO$_2$, see **Figure S2**. Inspection of the STEM images of MoO$_3$(15)/TiO$_2$ and Pt(3)MoO$_x$(15)/TiO$_2$ indicates that Mo species was highly dispersed on the TiO$_2$ surface. Moreover, the supported Pt was observed to be dispersed as nanoclusters/nanoparticles with an average diameter of 2.6 nm. As shown in **Figure S3**, energy dispersive spectroscopy (EDS) mapping was also carried out for Pt(3)/MoO$_x$(15)/TiO$_2$, confirming the high dispersion of Mo species and the presence of Pt nanoparticles.

Mo K-edge XAS measurements were conducted to identify the states of Mo species in the RWGS catalyst (**Figure S4**). The X-ray absorption near-edge structure (XANES) spectra showed that the shape and edge position for PtO$_2$(3)/MoO$_3$(15)/TiO$_2$ were identical to those observed for the reference MoO$_3$. For the Pt(3)/MoO$_x$(15)/TiO$_2$ sample, the absorption edge shifted toward lower energy, demonstrating the reduction of Mo species by the pretreatment with H$_2$. This result was confirmed by temperature programmed reduction (TPR) experiments using H$_2$ (**Figure S5**). A peak originating from the reduction of Pt species was observed around -10 °C. Our previous study on a similar material demonstrating that the Pt L$_3$-edge XANES of PtO/MoO$_3$/TiO$_2$ after H$_2$ reduction at r.t. was identical to that of metallic Pt foil corroborates this conclusion.[53] A relatively small peak can be seen in the H$_2$-TPR profile at around 270 °C. Since reduced Mo species were detected by XAS analysis of Pt(3)/MoO$_x$(15)/TiO$_2$, this peak was assigned to the reduction of Mo oxides. A very broad reduction peak around 400-600 °C and another reduction peak above 800 °C were also observed, indicating further reduction of the Mo species at those temperatures. These results suggest that Pt addition promotes reduction of Mo oxide species.

X-ray photoelectron spectroscopy (XPS) measurements were carried out to obtain further insights into the oxidation states of Mo. **Figure 2** shows the XPS spectra of the Mo 3d region of the sample before

and after H_2 reduction at 300 ˚C. The recorded XPS spectra for the Mo 3d region included signals from both $3d_{5/2}$ and $3d_{3/2}$ core levels for Mo. A $3d_{5/2}$ signal around a binding energy of 233.4 eV for $PtO_2(3)/MoO_3(15)/TiO_2$ (unreduced sample) was assigned to Mo^{6+}. On the other hand, the broad $3d_{5/2}$ peak for $Pt(3)/MoO_x(15)/TiO_2$ (reduced sample) indicated the presence of reduced Mo species that should appear at a binding energy lower than 232 eV. This is consistent with the result from Mo K-edge XAS measurements. Note that peaks corresponding to PtMo alloy and metallic Mo^0 (at around 228.7 eV) were hardly observed.[54,55] XPS spectra of the Pt 4f region have also been collected on samples without exposure to air (**Figure S6**). Peak centers of $4f_{7/2}$ signals for $Pt(3)/MoO_x/TiO_2$ (MoO_3 loading = 45, 15, and 7.5 wt%) and $Pt(3)/TiO_2$ were observed to be 71.6, 71.3, 71.1, and 70.8 eV. All these peaks can be assigned to metallic Pt,[56] which is consistent with the result from Pt L_3-edge XAS measurements. Although a negative shift was obserbed for $Pt(3)/TiO_2$ compared to the Pt $4f_{7/2}$ binding energy of bulk metallic Pt^0 (71.2 eV)[56] as observed previously for similar Pt/TiO_2 materials,[57–59] addition of Mo oxide species suppressed the negative shift. Note that this negative shift of Pt 4f region is thought to be originated from electron transfer from TiO_2 to Pt.[57,58]
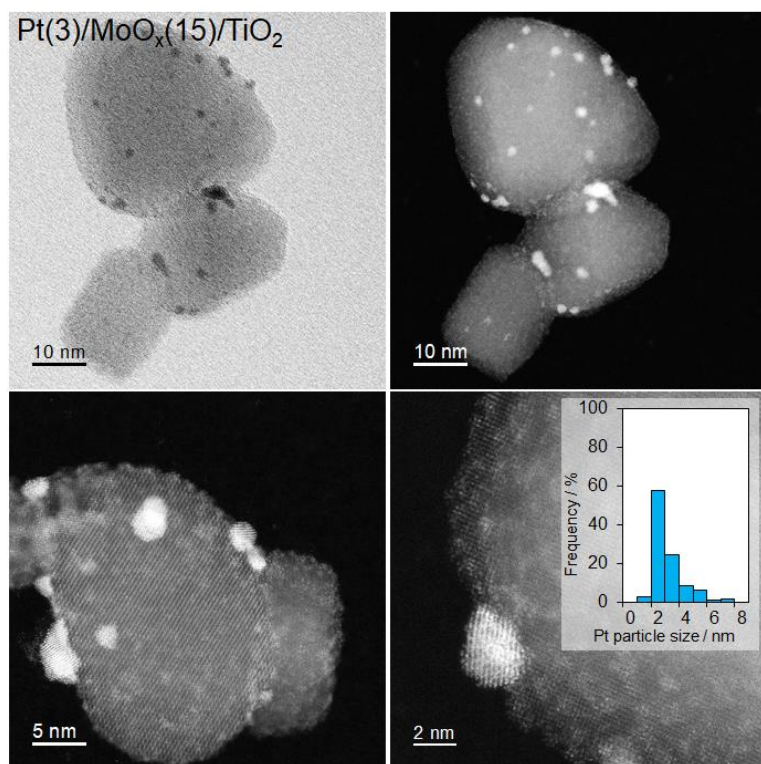

Figure 1. BF- and HAADF-STEM images for $Pt(3)/MoO_x(15)/TiO_2$ with the size distribution of Pt nanoparticles.
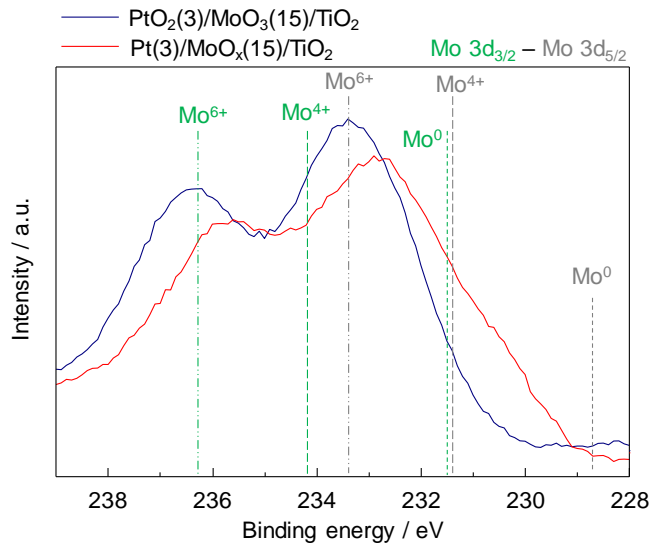
Figure 2. XPS spectra of the Mo 3d region of $PtO_2(3)/MoO_3(15)/TiO_2$ (unreduced sample; navy) and $Pt(3)/MoO_x(15)/TiO_2$ (reduced sample; red).

RWGS reaction

RWGS reactions were performed to investigate the properties of various catalysts. After pretreatment with H_2 at 300 °C, the reactions were carried out using 50 mg of a catalyst in a fixed bed continuous flow reactor under atmospheric pressure under the following composition of feed gas: 10 vol.% CO_2, 40 vol.% H_2, 45 vol.% He and 5 vol.% N_2 with a total flow rate of 100 cm^3 min^{-1}. The results are given in **Table 1**. $Pt(3)/MoO_x(15)/TiO_2$ afforded CO_2 conversion of 6.9% with 99.2% selectivity for CO and 0.8% selectivity for CH_4 (**entry 1**). In contrast, using $MoO_3(15)/TiO_2$ or other $MoO_x(15)/TiO_2$-supported metal catalysts (**entries 2-11**) did not give high CO_2 conversion. It was also found that the other supported metal catalysts show poor CO selectivity under the reaction condition employed. Ni and Ru, both of which are famous as methanation catalysts,[60,61] showed particularly low selectivity for CO formation. In addition to the unmodified support materials (**entries 12-19**), various metal oxides supported with species other than Mo oxide were screened (**entries 20-34**). $Pt(3)/VO_x(15)/TiO_2$ and $Pt(3)/CeO_x(15)/TiO_2$ showed comparable CO_2 conversion as the $Pt(3)/MoO_x(15)/TiO_2$-catalyzed system and even higher CO selectivity (100%) under the reaction conditions employed for this catalyst screening, while the other supported Pt catalysts showed inferior performances. Note that these Pt-based catalysts showed relatively high selectivity for CO formation regardless of the types of supports. It was found by control studies using supports other than TiO_2 (**entries 35-36**) that TiO_2 as a support in combination with Pt and MoO_x was effective for the RWGS process. Furthermore, commercial $Cu/ZnO/Al_2O_3$ catalysts as low-temperature WGS catalysts (MDC-7 and HiFUEL® W220, **entries 37** and **38**, respectively) and a commercial $FeCrCuO_x$ catalyst known as an Fe-Cr-based high-temperature WGS catalyst (HiFUEL® W210, **entry 39**)[62] were tested and found to be ineffective in this low temperature range.

For further investigation of the RWGS performance of some active catalysts ($Pt(3)/MO_x(15)/TiO_2$: M = Mo, V, and Ce), additional catalyst screening was conducted using a smaller amount of the catalyst (15 mg) to ensure the kinetic regime, as shown in **Figure 3**. Among the catalysts tested, $Pt(3)/MO_x(15)/TiO_2$ exhibited the best performance in all the temperature regions tested (200-300 °C). Note that CO selectivity was 100% for all the reaction systems. In addition, other TiO_2 supports having different crystal phases have also been tested under the same reaction condition at 250 °C. More specifically, STR-100N (Sakai Chemical Industry) having rutile phase with specific surface area of 100 m^2/g or ST-01 (Ishihara Sangyo) having anatase phase with specific surface area of 188 m^2/g has been used as a support instead of P25. $Pt(3)/MO_x(15)/TiO_2$ made with STR-100N and ST-01 gave CO yields of 5.0 and 3.3 % with 100% CO selectivity, respectively, while the $Pt(3)/MO_x(15)/TiO_2$ made with P25 gave 5.1% CO yield. As a result, we concluded that the combination of Pt, Mo oxides, and TiO_2 (P25) served as the best catalyst components for RWGS at 250 ˚C.

Table 1. Results of catalyst screening for the RWGS reaction.[a]

Entry	Catalyst	CO_2 conversion / %	Selectivity / % CO	CH$_4$
1	Pt(3)/MoO$_x$(15)/TiO$_2$	6.9	99.2	0.8
2	Rh(3)/MoO$_x$(15)/TiO$_2$	2.6	96.8	3.2
3	Ir(3)/MoO$_x$(15)/TiO$_2$	1.9	96.7	3.3
4	Ni(3)/MoO$_x$(15)/TiO$_2$	1.3	27.5	72.5
5	Re(3)/MoO$_x$(15)/TiO$_2$	0.9	90.4	9.6
6	Ru(3)/MoO$_x$(15)/TiO$_2$	0.8	12.4	87.6
7	Pd(3)/MoO$_x$(15)/TiO$_2$	0.5	98.0	2.0
8	Cu(3)/MoO$_x$(15)/TiO$_2$	<0.1	-	-
9	Ag(3)/MoO$_x$(15)/TiO$_2$	<0.1	-	-
10	Co(3)/MoO$_x$(15)/TiO$_2$	<0.1	-	-
11	MoO$_x$(15)/TiO$_2$	0.4	100	0
12	Pt(3)/CeO$_2$	5.9	100	0
13	Pt(3)/ZrO$_2$	5.3	99.6	0.4
14	Pt(3)/TiO$_2$	5.0	96.8	3.2
15	Pt(3)/Nb$_2$O$_5$	3.2	100	0
16	Pt(3)/MoO$_3$	1.8	100	0
17	Pt(3)/Al$_2$O$_3$	1.7	100	0
18	Pt(3)/SiO$_2$	1.5	100	0
19	Pt(3)/HZSM-5(22)	0.3	100	0
20	Pt(3)/VO$_x$/TiO$_2$	6.8	100	0
21	Pt(3)/CeO$_x$/TiO$_2$	6.7	100	0
22	Pt(3)/ZrO$_x$/TiO$_2$	4.1	97.6	2.4
23	Pt(3)/WO$_x$/TiO$_2$	3.8	100	0
24	Pt(3)/MgO$_x$/TiO$_2$	3.3	100	0
25	Pt(3)/NaO$_x$/TiO$_2$	3.2	100	0
26	Pt(3)/GeO$_x$/TiO$_2$	1.9	100	0
27	Pt(3)/MnO$_x$/TiO$_2$	1.8	100	0
28	Pt(3)/AlO$_x$/TiO$_2$	1.4	98.9	1.1
29	Pt(3)/SnO$_x$/TiO$_2$	0.9	100	0
30	Pt(3)/GaO$_x$/TiO$_2$	0.8	100	0
31	Pt(3)/CuO$_x$/TiO$_2$	0.2	100	0
33	Pt(3)/BiO$_x$/TiO$_2$	<0.1	-	-
34	Pt(3)/SbO$_x$/TiO$_2$	<0.1	-	-
35	Pt(3)/MoO$_x$/CeO$_2$	6.4	100	0
36	Pt(3)/MoO$_x$/Al$_2$O$_3$	2.5	100	0
37	Cu/ZnO/Al$_2$O$_3$ (MDC-7)	2.0	100	0
38	Cu/ZnO/Al$_2$O$_3$ (HiFUEL® W220)	1.8	100	0
39	FeCrCuO$_x$ (HiFUEL® W210)	1.2	95.5	4.5

[a]Catalyst (50 mg), CO_2:H$_2$:He:N$_2$ = 10:40:45:5 (N$_2$ as internal standard) with a flow rate of 100 mL min^{-1}, 250 °C.
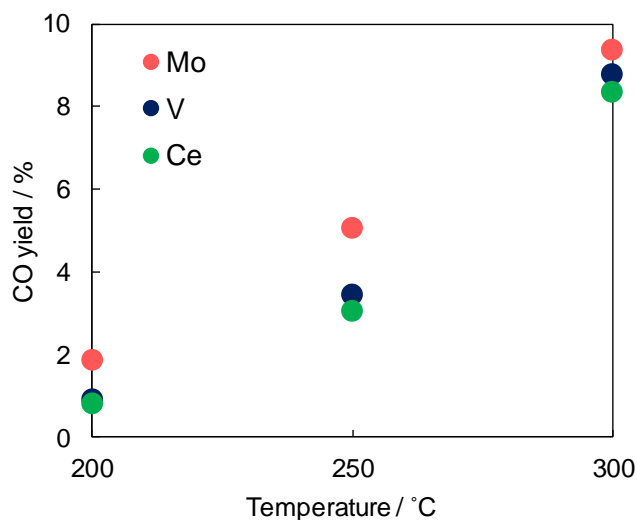
Figure 3. RWGS reaction over $Pt(3)/MoO_x(15)/TiO_2$, $Pt(3)/VO_x/TiO_2$, and $Pt(3)/CeO_x/TiO_2$. Catalyst (15 mg), $CO_2:H_2:He:N_2$ = 10:40:45:5, 100 mL min^{-1}.

With the best catalyst components in hand, the effects of the loading amount of Pt as well as Mo were investigated next (**Figure 4**). The selectivity toward CO formation decreased and a larger amount of CH_4 was formed when a $Pt/MoO_x/TiO_2$ catalyst containing a higher amount of Pt such as 10 wt% was employed. This indicates that larger Pt particles favor the CH_4 production over CO formation, which is in accordance with previous studies on RWGS over heterogeneous catalysts such as Rh/TiO_2,[63] Ni/SiO_2,[64,65] and Pt/TiO_2.[66] Moreover, the addition of Mo oxide species was found to have a large impact on the efficiency of CO generation and that loadings of 5-15 wt% Mo were optimal for the catalytic process considering both activity and selectivity. As a result, in this study, $Pt(3)/MoO_x(15)/TiO_2$ was identified to be the best for the RWGS process at 250 ˚C.

Using this optimized catalyst, kinetic studies were conducted. The Arrhenius plot (**Figure 5**) shows a linear slope in the applied temperature range (230-280 °C). Note that a lower catalyst amount was employed to ensure appropriate kinetic studies. The calculated apparent activation energy (Ea) was 30 kJ mol^{-1}. For comparison, the Arrhenius plot for the Pt/TiO_2 catalyst was obtained and the Ea was determined to be 49 kJ mol^{-1}. The change in Ea indicates a promotional effect of Mo species and suggests that the RWGS reaction proceeds through different reaction mechanisms. In addition, apparent reaction orders for CO_2, H_2, and CO were measured (**Table 2**). While the reaction orders for CO_2 and H_2 were not that different, the reaction order with respect to CO was significantly smaller for $Pt(3)/MoO_x(15)/TiO_2$ (-0.48) than $Pt(3)/TiO_2$ (-1.42), indicating a less inhibitory effect of CO for the $Pt(3)/MoO_x(15)/TiO_2$ catalyst. This result was further supported by *in situ* IR experiments using CO as a probe molecule (**Figure S7**). A significant amount of CO was adsorbed on $Pt(3)/TiO_2$ at 250 ˚C, whereas almost no CO was adsorbed on $Pt(3)/MoO_x(15)/TiO_2$ after purging with He.

A durability test was conducted next, as shown in **Figure 6**. The CO yield observed at the reaction time of 5 h was 4.1% and the corresponding CO formation rate was 1.11 mmol min^{-1} g^{-1}, which is the highest value reported so far below 250 °C (see **Table S1** for literature comparison). Note that the CO selectivity remained 100% throughout this durability test. Although the CO yield decreased over time, the CO formation rate after 600 h of the reaction time remained the best. It was also confirmed by using larger amount of the catalyst that the CO formation rate is high with 100% CO selectivity even at relatively high conversion region (0.66 mmol min^{-1} g^{-1} at CO_2 conversion of 9.4%). Therefore, our Pt(3)/MoO$_x$(15)/TiO$_2$ catalyst stands out as the state-of-the-art catalyst for the low-temperature RWGS reaction. To elucidate reasons of the catalyst deactivations, XRD and XAS measurements were performed for the Pt(3)/MoO$_x$(15)/TiO$_2$ catalyst after the long-term stability test (600 h RWGS reaction), as shown in **Figure S8**. No significant change was found in the XRD patterns where only peaks from TiO$_2$ were observed, indicating the absence of the crystalline species that are detectable by XRD except the TiO$_2$ support. Mo K-edge and Pt L$_3$-edge XANES were also identical, suggesting no significant changes on states of Pt and Mo species. In contrast, curve-fitting analysis of the Pt L$_3$-edge EXAFS demonstrated that the coordination number of Pt–Pt bond became larger from 5.5 to 6.0 (**Table 3**). This result indicates that Pt particles were aggregated to form larger particles during the RWGS reaction, and this aggregation would be a reason for the activity loss observed. It should also be noted that formation of Pt–Mo bimetals can also be a possible reason for the deactivation[53,67] although there is no obvious clue for the formation of such species. In addition, temperature-programmed oxidation (TPO) measurement was performed in order to check possibility of coke deposition during the long-term stability test. No coke formation was found for the spent Pt(3)/MoO$_x$(15)/TiO$_2$ catalyst.
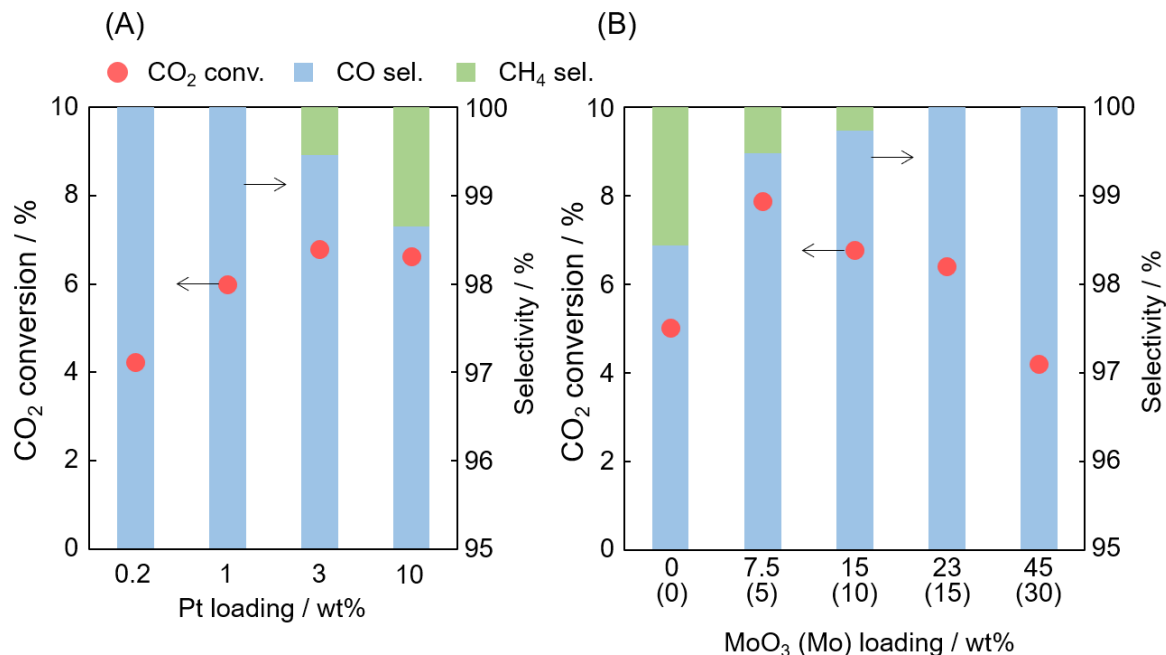
Figure 4. Effect of the loading amount of (A) Pt and (B) MoO_3 (Mo) on the RWGS reaction for $Pt/MoO_x/TiO_2$. $CO_2:H_2:He:N_2 = 10:40:45:5$, 100 mL min^{-1}, 250 °C. Catalyst amount was adjusted to contain 0.5 mg of Pt. 15 wt% MoO_3 loading was used for investigations on the effect of Pt loading while 3 wt% Pt loading was used for investigations on the effect of MoO_3 loading.
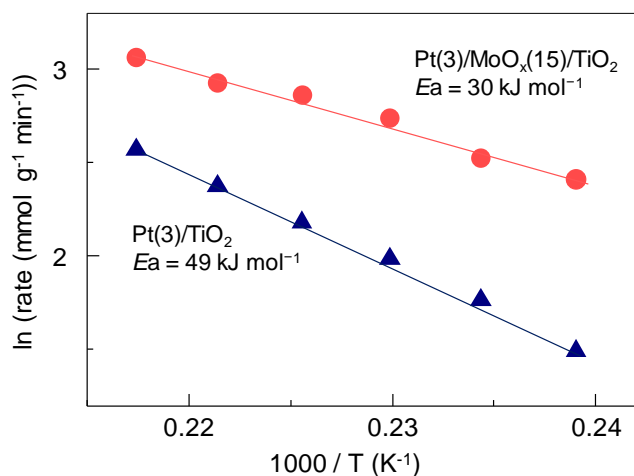

Figure 5. Arrhenius plot for the RWGS reaction over $Pt(3)/MoO_x(15)/TiO_2$ and $Pt(3)/TiO_2$. Catalyst (5 mg), $CO_2:H_2:He:N_2 = 10:40:45:5$, 100 mL min^{-1}, 230-280 °C.

Table 2. Reaction orders for the RWGS reaction over $Pt(3)/MoO_x(15)/TiO_2$ and $Pt(3)/TiO_2$.

Catalyst	CO_2	H_2	CO
$Pt(3)/MoO_x(15)/TiO_2$	0.36	0.26	-0.48
$Pt(3)/TiO_2$	0.51	0.20	-1.42

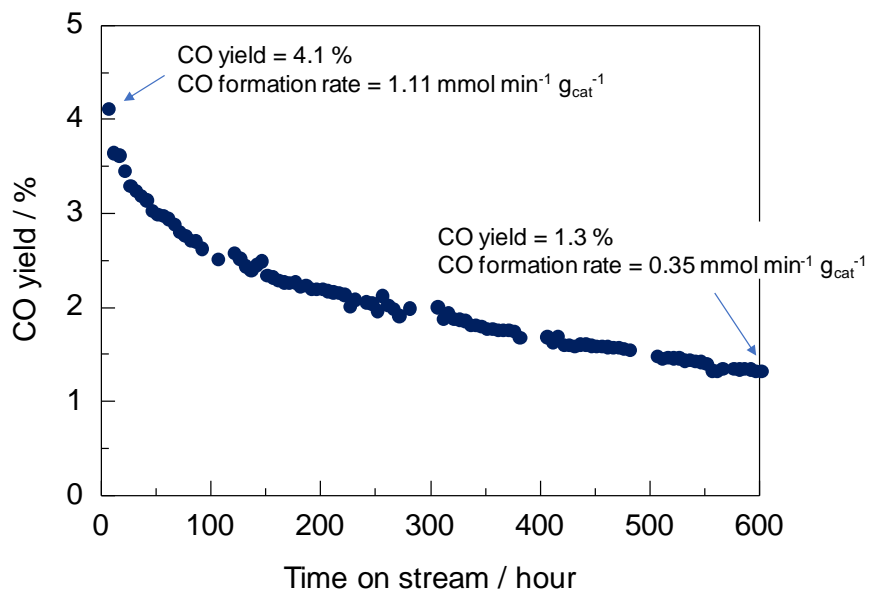Catalyst (5 mg), $CO_2:H_2:He:N_2 = 10:40:45:5$, 100 mL min^{-1}, 250 °C.

11

Figure 6. Long-term stability test for the RWGS reaction over Pt(3)/MoO$_x$(15)/TiO$_2$. Reaction conditions: catalyst (15 mg), CO$_2$:H$_2$:He:N$_2$ = 10:40:45:5, 100 mL min^{-1}, 250 °C.

Table 3. Pt L$_3$-edge EXAFS curve fitting analysis for the Pt(3)/MoO$_x$(15)/TiO$_2$ before (fresh) and after the 600 h reaction (spent).

Catalyst	Shell	Coordination number	Bond distance (Å)	Debye-Waller factor (Å)	Residual factor (%)
Fresh	Pt–Pt	5.5	2.76	0.008	0.8
Spent	Pt–Pt	6.0	2.75	0.007	0.6

Mechanistic Study

Two major reaction mechanisms are known for the RWGS reaction.[68] They include (i) the redox mechanism and (ii) the associative mechanism. In the former, oxygen vacancies are formed on the oxide (support) surface by H_2, which acts as a reducing agent without direct participation in the intermediates formation processes. CO_2 reoxidizes the partially reduced oxide to fill the formed oxygen vacancies (so-called reverse Mars−van Krevelen mechanism[69]), resulting in the formation of CO. In the latter mechanism, CO is produced through decomposition of surface-reactive intermediates such as formate, carbonate, and carboxyl species, which can be derived from the reaction of hydrogen species with CO_2.[70–73]

To clarify the reaction mechanism, *operando* XANES measurements were conducted under a flow of CO_2, H_2, CO_2+H_2 at 250 °C. Simultaneous analysis of the gas phase products was performed using gas chromatography (GC). For that purpose, 10%CO_2/He, 40%H_2/He, and 10%CO_2+40%H_2/He were introduced consecutively with an interval of He purge prior to the CO_2 introduction. For *operando* Mo K-edge XANES measurements, the weight/volumetric flow rate (W/F) ratios were set to be similar to the reaction conditions employed in **Figure 3**. **Figure 7A** shows the corresponding Mo K-edge XANES of Pt(3)/MoO$_x$(15)/TiO$_2$ measured just after the pretreatment and under a 10%CO_2/He flow. The XANES of Pt(3)/MoO$_x$(15)/TiO$_2$ shows that the absorption edge shifted to higher energy by the CO_2 introduction. Simultaneously, CO was detected by GC. Mass spectrometry was used to confirm that the remaining H_2 in the gas lines was completely evacuated by the He purge. Therefore, these results clearly demonstrate that CO_2 acted as an oxidant, and as a result Mo species were oxidized. More specifically, the surface defect sites induced by the H_2 reduction played an important role for the CO formation. Subsequently, the partly oxidized MoO$_x$ species were reduced by H_2 introduced, as shown in **Figure 7B**. It is noteworthy that CO formation was not detected upon the introduction of 40%H_2/He, suggesting that H_2 does not participate in the CO formation process, but rather contributes to the formation of oxygen vacancy sites where CO_2 is reduced to CO. Moreover, the edge position for the Mo species remained almost unchanged during the RWGS condition (10%CO_2+40%H_2/He).

Operando Ti K-edge and Pt L$_3$-edge XANES spectra were also obtained employing the same protocol described above, except for amounts of the samples and gas flow rates, in order to obtain good XAS spectra with the transmission measurements (**Figure S9**). The edge positions for both Ti K-edge and Pt L$_3$-edge XANES spectra were hardly changed following the introduction of CO_2, suggesting that the redox of TiO$_2$ and Pt was not directly involved in the RWGS reaction.

Operando diffuse reflectance infrared Fourier transform spectroscopy (DRIFTS) was also performed to investigate surface adsorbed species that can potentially be involved in the reaction. DRIFT spectra obtained at 250 °C after the H_2 reduction pretreatment and after subsequent introduction of 100%

CO_2 are given in **Figure S10**. A band at around 2078 cm^{-1}, which can be assigned to CO adsorbed on metallic Pt, was seen immediately after the introduction of 100% CO_2. Simultaneous formation of CO in the gas phase was also observed by using an IR gas cell equipped at outlet of the DRIFT cell. Although a small band at around 1508 cm^{-1}, which can be assigned to carbonate species,[68] appeared gradually, the evolution trend of this band does not match the trend of the CO formation in the gas phase. This result indicates that surface adsorbed species are not involved in the RWGS reaction over Pt(3)/MoO$_x$(15)/TiO$_2$. These results coming from *operando* XAS and DRIFT indicate that the RWGS process over Pt(3)/MoO$_x$(15)/TiO$_2$ proceeds through a regenerative redox mechanism in which supported Mo species undergo redox by CO_2 and H_2 as oxidizing and reducing substrates, respectively.
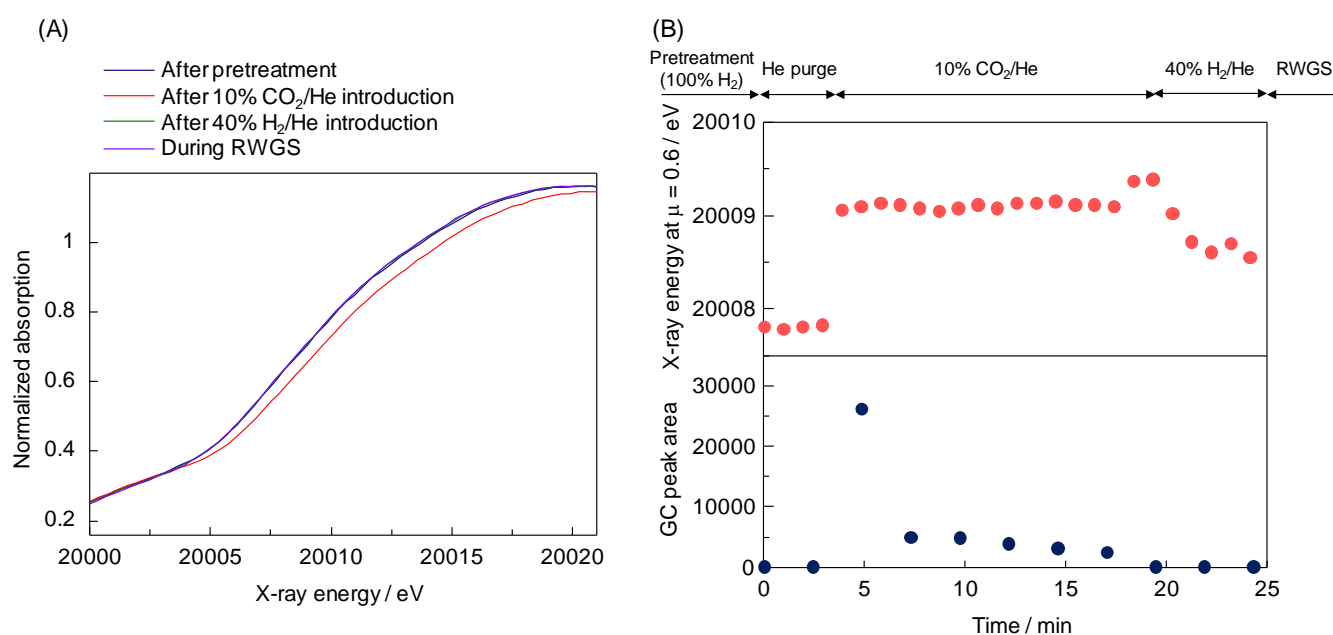

Figure 7. (A) *Operando* Mo K-edge XANES of Pt(3)/MoO$_x$(15)/TiO$_2$ obtained at 250 °C after the H_2 reduction pretreatment (navy blue line) and after subsequent introduction of 10%CO_2/He (red line). (B) Results of the *operando* Mo K-edge XAS measurements. Changes in the shift of the absorption edge and the amount of CO in the gas phase (GC peak area) under flowing 10%CO_2/He, 40%H_2/He, and 10%CO_2+40%H_2/He at 250 °C.

Conclusions

The catalytic RWGS reaction was carried out at 250 °C under ambient pressure employing a Pt(3)/MoO$_x$(15)/TiO$_2$ catalyst and various other catalysts that include MoO$_x$(15)/TiO$_2$-supported and oxide-supported catalysts as well as commercially available Cu/ZnO/Al$_2$O$_3$ and Fe-Cr-based catalysts. Pt(3)/MoO$_x$(15)/TiO$_2$ showed the best performance in terms of CO productivity among the catalysts tested. The reduced MoO$_x$ species was identified by *operando* XAS studies as playing an important role in reducing CO$_2$. Employing metal oxide species that show efficient redox properties toward reactions with CO$_2$ and H$_2$ at working temperatures would be a key to realizing efficient RWGS catalytic processes.

## Conflicts of interest

There are no conflicts to declare

REFERENCES

1   A. Álvarez, A. Bansode, A. Urakawa, A. V. Bavykina, T. A. Wezendonk, M. Makkee, J. Gascon and F. Kapteijn, *Chem. Rev.*, 2017, **117**, 9804–9838.
2   S. Dabral and T. Schaub, *Adv. Synth. Catal.*, 2019, **361**, 223–246.
3   J. R. Cabrero-Antonino, R. Adam and M. Beller, *Angew. Chemie - Int. Ed.*, 2019, **58**, 12820–12838.
4   R. P. Ye, J. Ding, W. Gong, M. D. Argyle, Q. Zhong, Y. Wang, C. K. Russell, Z. Xu, A. G. Russell, Q. Li, M. Fan and Y. G. Yao, *Nat. Commun.*, 2019, **10**, 5698.
5   E. C. Ra, K. Y. Kim, E. H. Kim, H. Lee, K. An and J. S. Lee, *ACS Catal.*, 2020, **2020**, 11318–11345.
6   P. Gao, L. Zhang, S. Li, Z. Zhou and Y. Sun, *ACS Cent. Sci.*, 2020, **6**, 1657−1670.
7   C. Vogt, M. Monai, E. B. Sterk, J. Palle, A. E. M. Melcherts, B. Zijlstra, E. Groeneveld, P. H. Berben, J. M. Boereboom, E. J. M. Hensen, F. Meirer, I. A. W. Filot and B. M. Weckhuysen, *Nat. Commun.*, 2019, **10**, 5330.
8   M. D. Burkart, N. Hazari, C. L. Tway and E. L. Zeitler, *ACS Catal.*, 2019, **9**, 7937−7956.
9   J. Artz, T. E. Müller, K. Thenert, J. Kleinekorte, R. Meys, A. Sternberg, A. Bardow and W. Leitner, *Chem. Rev.*, 2018, **118**, 434–504.
10   A. Ramirez, S. M. Sarathy and J. Gascon, *Trends Chem.*, 2020, **2**, 785–795.
11   A. Parastaev, V. Muravev, E. Huertas Osta, A. J. F. van Hoof, T. F. Kimpel, N. Kosinov and E. J. M. Hensen, *Nat. Catal.*, 2020, **3**, 526–533.
12   W. H. Wang, Y. Himeda, J. T. Muckerman, G. F. Manbeck and E. Fujita, *Chem. Rev.*, 2015, **115**, 12936–12973.
13   M. Ronda‑Lloret, G. Rothenberg and N. R. Shiju, *ChemSusChem*, 2019, **12**, 3896–3914.
14   J. Bao, G. Yang, Y. Yoneyama and N. Tsubaki, *ACS Catal.*, 2019, **9**, 3026−3053.
15   W. Zhou, K. Cheng, J. Kang, C. Zhou, V. Subramanian, Q. Zhang and Y. Wang, *Chem. Soc. Rev.*, 2019, **48**, 3193–3228.
16   S. Kar, A. Goeppert and G. K. S. Prakash, *Acc. Chem. Res.*, 2019, **52**, 2892−2903.
17   J. Zhong, X. Yang, Z. Wu, B. Liang, Y. Huang and T. Zhang, *Chem. Soc. Rev.*, 2020, **49**, 1385–1413.
18   X. Jiang, X. Nie, X. Guo, C. Song and J. G. Chen, *Chem. Rev.*, 2020, **15**, 7984–8034.
19   J. Zhang, S. Deo, M. J. Janik and J. Will Medlin, *J. Am. Chem. Soc.*, 2020, **142**, 5184–5193.
20   M. Heenemann, M. M. Millet, F. Girgsdies, M. Eichelbaum, T. Risse, R. Schlögl, T. Jones and E. Frei, *ACS Catal.*, 2020, **10**, 5672−5680.
21   M. Zhu, P. Tian, M. E. Ford, J. Chen, J. Xu, Y. F. Han and I. E. Wachs, *ACS Catal.*, 2020, **10**, 7857−7863.
22   M. Zabilskiy, V. L. Sushkevich, D. Palagin, M. A. Newton, F. Krumeich and J. A. van Bokhoven, *Nat. Commun.*, 2020, **11**, 2409.
23   Y. Kuwahara, Y. Fujie, T. Mihogi and H. Yamashita, *ACS Catal.*, 2020, **10**, 6356–6366.
24   Q. Sun, B. W. J. Chen, N. Wang, Q. He, A. Chang, C. M. Yang, H. Asakura, T. Tanaka, M. J. Hülsey, C. H. Wang, J. Yu and N. Yan, *Angew. Chemie - Int. Ed.*, 2020, **59**, 20183–20191.
25   P. Gao, S. Li, X. Bu, S. Dang, Z. Liu, H. Wang, L. Zhong, M. Qiu, C. Yang, J. Cai, W. Wei and Y. Sun, *Nat. Chem.*, 2017, **9**, 1019–1024.
26   D. U. Nielsen, X. M. Hu, K. Daasbjerg and T. Skrydstrup, *Nat. Catal.*, 2018, **1**, 244–254.
27   M. D. Porosoff, B. Yan and J. G. Chen, *Energy Environ. Sci.*, 2016, **9**, 62–73.
28   H. T. Luk, C. Mondelli, D. C. Ferré, J. A. Stewart and J. Pérez-Ramírez, *Chem. Soc. Rev.*, 2017, **46**, 1358–1426.
29   J. Kang, S. He, W. Zhou, Z. Shen, Y. Li, M. Chen, Q. Zhang and Y. Wang, *Nat. Commun.*, 2020, **11**, 827.
30   J. Li, Y. He, L. Tan, P. Zhang, X. Peng, A. Oruganti, G. Yang, H. Abe, Y. Wang and N. Tsubaki, *Nat. Catal.*, 2018, **1**, 787–793.
31   B. Zijlstra, R. J. P. Broos, W. Chen, G. L. Bezemer, I. A. W. Filot and E. J. M. Hensen, *ACS Catal.*, 2020, **10**, 9376–9400.
32   P. Zhang, L. Tan, G. Yang and N. Tsubaki, *Chem. Sci.*, 2017, **8**, 7941–7946.
33   X. Xiaoding and J. A. Moulijn, *Energy and Fuels*, 1996, **10**, 305–325.
34   F. S. Stone and D. Waller, *Top. Catal.*, 2003, **22**, 305–318.
35   A. Goguet, F. C. Meunier, D. Tibiletti, J. P. Breen and R. Burch, *J. Phys. Chem. B*, 2004, **108**, 20240–20246.
36   J. A. Rodriguez, J. Evans, L. Feria, A. B. Vidal, P. Liu, K. Nakamura and F. Illas, *J. Catal.*, 2013, **307**, 162–169.

37   R. Carrasquillo-Flores, I. Ro, M. D. Kumbhalkar, S. Burt, C. A. Carrero, A. C. Alba-Rubio, J. T. Miller, I. Hermans, G. W. Huber and J. A. Dumesic, *J. Am. Chem. Soc.*, 2015, **137**, 10317−10325.
38   J. A. Loiland, M. J. Wulfers, N. S. Marinkovic and R. F. Lobo, *Catal. Sci. Technol.*, 2016, **6**, 5267–5279.
39   X. Su, X. Yang, B. Zhao and Y. Huang, *J. Energy Chem.*, 2017, **26**, 854–867.
40   S. C. Yang, S. H. Pang, T. P. Sulmonetti, W. N. Su, J. F. Lee, B. J. Hwang and C. W. Jones, *ACS Catal.*, 2018, **8**, 12056−12066.
41   A. M. Bahmanpour, F. Héroguel, M. Kıllç, C. J. Baranowski, L. Artiglia, U. Röthlisberger, J. S. Luterbacher and O. Kröcher, *ACS Catal.*, 2019, **9**, 6243−6251.
42   X. Chen, Y. Chen, C. Song, P. Ji, N. Wang, W. Wang and L. Cui, *Front. Chem.*, 2020, **8**, 709.
43   D. Vovchok, C. Zhang, S. Hwang, L. Jiao, F. Zhang, Z. Liu, S. D. Senanayake and J. A. Rodriguez, *ACS Catal.*, 2020, **10**, 10216−10228.
44   I. Ro, C. Sener, T. M. Stadelman, M. R. Ball, J. M. Venegas, S. P. Burt, I. Hermans, J. A. Dumesic and G. W. Huber, *J. Catal.*, 2016, **344**, 784–794.
45   Y. F. Li, W. Lu, K. Chen, P. Duchesne, A. Jelle, M. Xia, T. E. Wood, U. Ulmer and G. A. Ozin, *J. Am. Chem. Soc.*, 2019, **141**, 14991−14996.
46   Y. F. Xu, P. N. Duchesne, L. Wang, A. Tavasoli, A. A. Jelle, M. Xia, J. F. Liao, D. Bin Kuang and G. A. Ozin, *Nat. Commun.*, 2020, **11**, 5149.
47   L. Wang, Y. Dong, T. Yan, Z. Hu, A. A. Jelle, D. M. Meira, P. N. Duchesne, J. Y. Y. Loh, C. Qiu, E. E. Storey, Y. Xu, W. Sun, M. Ghoussoub, N. P. Kherani, A. S. Helmy and G. A. Ozin, *Nat. Commun.*, 2020, **11**, 2432.
48   Y. Qi, L. Song, S. Ouyang, X. Liang, S. Ning, Q. Q. Zhang and J. Ye, *Adv. Mater.*, 2020, **32**, 1903915.
49   A. Mohan, U. Ulmer, L. Hurtado, J. Loh, Y. F. Li, A. A. Tountas, C. Krevert, C. Chan, Y. Liang, P. Brodersen, M. M. Sain and G. A. Ozin, *ACS Appl. Mater. Interfaces*, 2020, **12**, 33613−33620.
50   K. Shimizu, W. Onodera, A. S. Touchy, S. M. A. H. Siddiki, T. Toyao and K. Kon, *ChemistrySelect*, 2016, **1**, 736–740.
51   T. Toyao, S. M. A. Hakim Siddiki, K. Kon and K. Shimizu, *Chem. Rec.*, 2018, **18**, 1374–1393.
52   T. Toyao, S. M. A. H. Siddiki, K. Ishihara, K. Kon, W. Onodera and K. Shimizu, *Chem. Lett.*, 2017, **46**, 68–70.
53   T. Toyao, S. Kayamori, Z. Maeno, S. M. A. H. Siddiki and K. Shimizu, *ACS Catal.*, 2019, **9**, 8187–8196.
54   S. Zafeiratos, G. Papakonstantinou, M. M. Jacksic and S. G. Neophytides, *J. Catal.*, 2005, **232**, 127–136.
55   A. Katrib, J. W. Sobczak, M. Krawczyk, L. Zommer, A. Benadda, A. Jablonski and G. Maire, *Surf. Interface Anal.*, 2002, **34**, 225–229.
56   L. Nie, J. Yu, X. Li, B. Cheng, G. Liu and M. Jaroniec, *Environ. Sci. Technol.*, 2013, **47**, 2777–2783.
57   J. Yu, L. Qi and M. Jaroniec, *J. Phys. Chem. C*, 2010, **114**, 13118–13125.
58   X. Zhu, B. Cheng, J. Yu and W. Ho, *Appl. Surf. Sci.*, 2016, **364**, 808–814.
59   H. Huang and D. Y. C. Leung, *J. Catal.*, 2011, **280**, 60–67.
60   S. Tada, S. Ikeda, N. Shimoda, T. Honma, M. Takahashi, A. Nariyuki and S. Satokawa, *Int. J. Hydrogen Energy*, 2017, **42**, 30126–30134.
61   H. Nagase, R. Naito, S. Tada, R. Kikuchi, K. Fujiwara, M. Nishijima and T. Honma, *Catal. Sci. Technol.*, 2020, **10**, 4522–4531.
62   M. Juneau, M. Vonglis, J. Hartvigsen, L. Frost, D. Bayerl, M. Dixit, G. Mpourmpakis, J. R. Morse, J. W. Baldwin, H. D. Willauer and M. D. Porosoff, *Energy Environ. Sci.*, 2020, **13**, 2524–2539.
63   J. C. Matsubu, V. N. Yang and P. Christopher, *J. Am. Chem. Soc.*, 2015, **137**, 3076–3084.
64   H. C. Wu, Y. C. Chang, J. H. Wu, J. H. Lin, I. K. Lin and C. S. Chen, *Catal. Sci. Technol.*, 2015, **5**, 4154–4163.
65   M. M. Millet, G. Algara-Siller, S. Wrabetz, A. Mazheika, F. Girgsdies, D. Teschner, F. Seitz, A. Tarasov, S. V. Levchenko, R. Schlögl and E. Frei, *J. Am. Chem. Soc.*, 2019, **141**, 2451−2461.
66   X. Chen, X. Su, H. Duan, B. Liang, Y. Huang and T. Zhang, *Catal. Today*, 2017, **281**, 312–318.
67   P. J. Dietrich, R. J. Lobo-Lapidus, T. Wu, A. Sumer, M. C. Akatay, B. R. Fingland, N. Guo, J. A. Dumesic, C. L. Marshall, E. Stach, J. Jellinek, W. N. Delgass, F. H. Ribeiro and J. T. Miller, *Top. Catal.*, 2012, **55**, 53–69.
68   L. F. Bobadilla, J. L. Santos, S. Ivanova, J. A. Odriozola and A. Urakawa, *ACS Catal.*, 2018, **8**, 7455−7467.
69   A. V. Mironenko and D. G. Vlachos, *J. Am. Chem. Soc.*, 2016, **138**, 8104–8113.
70   D. Heyl, U. Rodemerck and U. Bentrup, *ACS Catal.*, 2016, **6**, 6275−6284.
71   D. Ma and C. R. F. Lund, *Ind. Eng. Chem. Res.*, 2003, **42**, 711–717.

72   N. C. Nelson, M. T. Nguyen, V. A. Glezakou, R. Rousseau and J. Szanyi, *Nat. Catal.*, 2019, **2**, 916–924.

73   N. C. Nelson and J. Szanyi, *ACS Catal.*, 2020, **10**, 5663−5671.

Table of Contents Entry
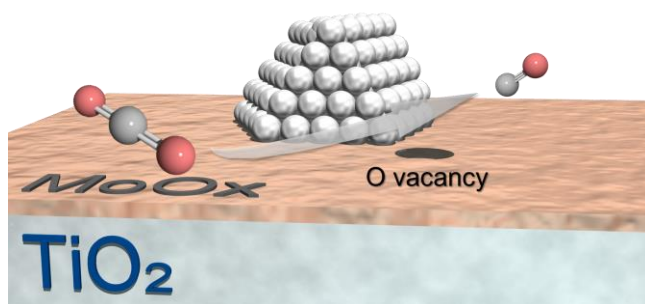
Pt/MoO$_X$/TiO$_2$ shows excellent catalytic performance for the reverse water-gas shift reaction at 250 ˚C via reverse Mars−van Krevelen mechanism.